IDE∆L®

Single-Point Magnetic Resonance Imaging Study of Water Adsorption in Pellets of Zeolite 4A

Pablo J. Prado,* Bruce J. Balcom,*,1 and Mohamed Jama†

*MRI Centre, Department of Physics; and †Chemical Engineering Department, University of New Brunswick,
P.O. Box 4400, Fredericton, New Brunswick, Canada E3B 5A3

The water uptake process in commercial type particles of zeolite 4A has been studied using a single-point MRI method. True proton density, T_1, T_2, and T_2^* relaxation times were obtained with submillimetric resolution, overcoming the restrictions of short T_2^* signals. The molecular mobility in nonequilibrium conditions has been characterized by relaxation time mapping. A clear reduction of the water sorption rate was observed by comparing MRI profiles of a loosely packed bed and gravimetric measurements of spread particles from the same sieved zeolite batch. © 1999 Academic Press

INTRODUCTION

Fluid uptake in microporous solids is a process of general industrial importance (*1, 2*). Zeolites, one type of microporous material, are used in separation processes and as catalysts and drying agents. In particular, zeolite 4A is an efficient absorbent for molecules with an effective size under 4×10^{-10} m. Its water capacity is 22–22 wt% (*1*), but oxygen and nitrogen are not adsorbed (*3*). As a result, zeolite 4A is widely used as a drying agent for natural gas, liquid paraffins, and organic solvents.

In order to attain information on diffusional resistance mechanisms in porous adsorbents, numerous techniques have been proposed (see, for example, (*4*)). The time evolution of the adsorbate distribution in a zeolite reflects the different diffusional driving forces. Kärger *et al.* (*2, 5, 6*) have reported the use of magnetic resonance imaging (MRI) combined with pulsed field gradient NMR (*7–9*) to observe the proton distribution and molecular diffusion during sorption processes in a zeolite bed.

The strong interaction between the adsorbed molecules and the porous solid results in efficient spin–spin and spin–lattice relaxation. These processes depend on paramagnetic impurities and heterogenous magnetic susceptibility which varies greatly with zeolite preparation. Even though some adsorbate–adsorbent systems can be studied by conventional MRI (*10*), short spin–spin relaxation times impose restrictions on the imaging resolution and sensitivity. Diffusants under restricted motion in

the zeolite intracrystalline spaces can have transverse relaxation times under 100 μs (*11*). Furthermore, interactions of polar molecules with the adsorbent surface reduce the T_2 time constant and intracrystalline diffusion coefficients. Relaxation time changes with temperature may limit the range of applicability of a particular imaging technique, as in the case of *n*-hexane in NaX zeolite, where T_2 is a few milliseconds at room temperature but decreases to less than 100 μs at 130 K (*12*).

Various MRI methods have been devoted to investigate short T_2^* systems. Stray field imaging (*13*) and oscillating field gradient (*14–16*) techniques have been used to study porous media. In the present work we use the single-point-imaging (SPI) technique (*17*), which has been successful for studying a range of short relaxation time systems (*18–20*). Applications to high resolution MRI microscopy have been described by Choi *et al.* (*21*), while Gravina and Cory (*22*) have discussed its sensitivity and resolution characteristics. Beyea *et al.* (*23*) investigated the moisture content in concrete materials using this method.

The inherently long acquisition time of SPI has been overcome by a novel pulse sequence, namely single-point ramped imaging with T_1 enhancement, SPRITE (*24*). A dramatic time improvement allows for fast signal averaging, and consequently a significant signal-to-noise ratio, SNR, increase. Moreover, in this work SPRITE-T_2^* and SPI-T_1 and T_2 relaxation time maps are obtained with submillimetric resolution, permitting a quantitative determination of proton density and a spatially resolved observation of the diffusant molecular dynamics. This is important when describing a nonequilibrated hydration process or imaging of gases at different environments, presenting different relaxation times (*25*). To the best of our knowledge, this is the first relaxation time mapping report of short T_2^* zeolite systems. A number of imaging experiments on porous media (*20*), gases, and solids (*26*) have demonstrated the extensive applications of this imaging technique, even with systems presenting transverse relaxation times well under 100 μs.

Broad-line MRI studies of water uptake into zeolite 4A powder beds have been reported (*27–29*) and the slow hydra-

---

tion process has been modeled (*3*). An SPI-based investigation of the phenomenon is now introduced. In the results section, a brief discussion of water mobility is presented based on the space-dependent characteristics of the relaxation times.

SPI RELAXOMETRY

SPI is a pure phase encoding MRI technique. The signal is acquired at $t = t_p$ after a short excitation pulse in the presence of magnetic field gradients. Then, in contrast to conventional MRI, the k-space trajectory is defined by changes in the gradient with a constant phase encoding time. A detailed discussion on SPI–SPRITE relaxometry, pulse sequences, and signal processes has been presented elsewhere (*19, 20*). The Fourier transformation of the measured signal produces a relaxation-weighted profile:

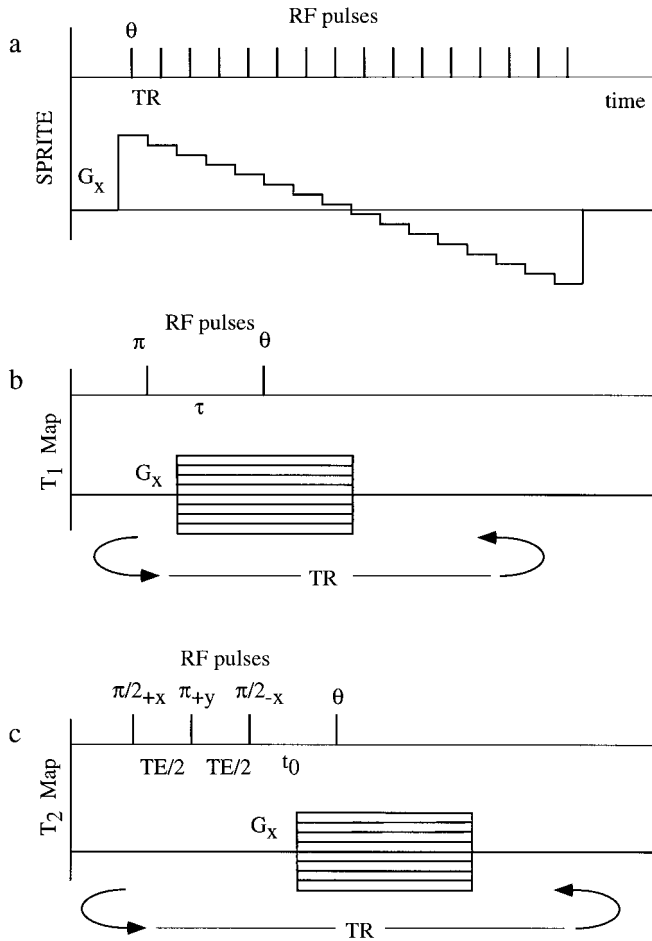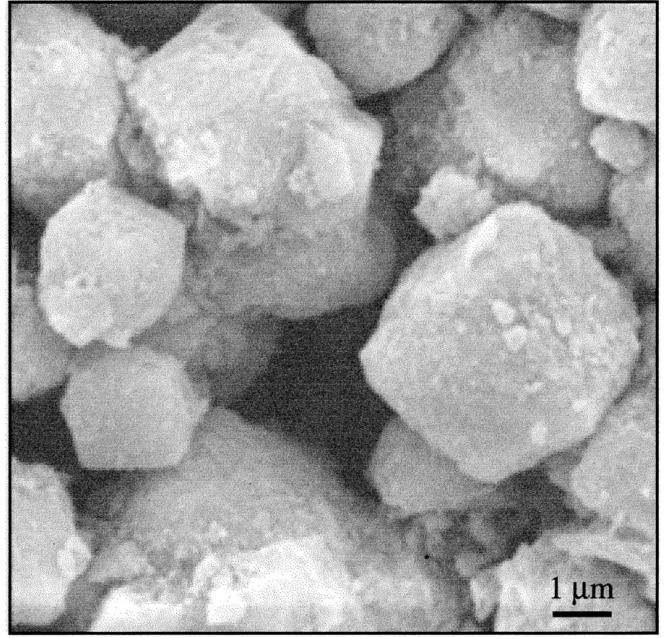$$\rho(x) = R(x)\exp[-t_p/T_2^*(x)]\rho_0(x). \qquad [1]$$

FIG. 2. Scanning electron micrograph of crushed industrial grade zeolite 4A used in the present study.

$\rho_0(x)$ is the true unidimensional spin density distribution. The relaxation factor, $R(x)$, reflects contributions from preparation pulses and saturation effects. Pulse sequence manipulation may introduce relaxation time contrast in heterogeneous systems (*19, 20*). If saturation effects are avoided and no preparation pulses are introduced, $R(x) = 1$. Equation [1] demonstrates that for a heterogeneous system, T_2^*-value mapping is necessary in order to calculate the true spin density.

For a SPRITE experiment, where the magnetic field gradient is changed in a stepwise manner (Fig. 1a), saturation effects must be carefully evaluated because the gradient ramp speed is limited by the longest T_1 component of the sample and the excitation pulse duration. A low flip angle excitation pulse partially compensates for long T_1 signal recovery.

A spatially resolved T_1 measurement is achieved with an inversion pulse and variable delay time prior to the SPI sampling pulse (Fig. 1b). The gradient is switched on between the π-pulse and the sampling pulse. Each k-space point is individually prepared with an inversion pulse and variable delay. A double exponential recovery can be represented by the relaxation factor:

$$R^{T_1}(x) = 1 - A_S\exp[-\tau/T_{1S}(x)]$$
$$- A_L\exp[-\tau/T_{1L}(x)], \qquad [2]$$

where A_S and A_L are the relative contributions from short (T_{1S}) and long (T_{1L}) recovery components, respectively.

T_2 mapping is obtained by SPI with a Carr–Purcell preparation sequence: $\pi/2_{+x}$–TE/2–π_{+y}–TE/2–$\pi/2_{-x}$–t_0–SPI,

FIG. 1. One-dimensional relaxation time mapping single-point imaging pulse sequences. (a) Single-point ramped imaging with T_1 enhancement, SPRITE. (b) Inversion recovery SPI-T_1 map. (c) Spin echo SPI-T_2 map. 20 G/cm maximum gradient amplitudes and $t_p = 100$ μs phase encoding times were used in (b) and (c).
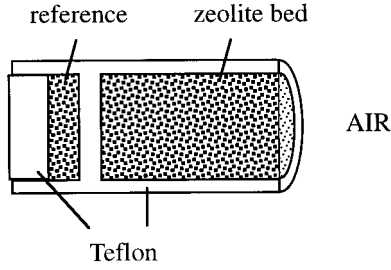
FIG. 3. Experimental zeolite sample (20–40 mesh) and holder. The open end was covered with a thin cloth, and the reference side was closed to keep a constant adsorbate level. Sample and reference total length was 28 mm.

with the gradient switched on during the waiting time t_0 (Fig. 1c). The extra pulse at the echo time, TE, z-stores the T_2 modulated transverse magnetization and allows for echo times shorter than the gradient rise time. Each k-space point is individually weighted by the spin echo modulated transverse magnetization. Recovery of magnetization during t_0 introduces T_1 weighting to the measured signal. The relaxation factor reflects both T_1 and T_2 contributions:

$$R^{T_2}(x) - A \exp[-TE/T_2(x)] + B, \qquad [3]$$

where the coefficients A and B are functions of T_1 and t_0, but not TE.

T_2^* mapping with SPRITE is achieved by systemically varying the encoding time t_p while maintaining a constant field of view (FOV) through concomitant changes in the phase encode gradients. Neglecting saturation effects and without influence from preceding pulses, Eq. [1] becomes simply

$$\rho(x) = \exp[-t_p/T_2^*(x)]\rho_0(x), \qquad [4]$$

and T_2^* can be determined with an exponential fit at any spatial position.

For the parameters used in this phase encoding study, the signal loss factor due to diffusion in the presence of magnetic field gradients (22, 30), $\exp(-\frac{1}{3}\gamma^2 G^2 D t_p^3)$ is insignificant. Even though the maximum gradient $G = 20$ G/cm is higher than with conventional spin-echo methods, encoding times under 100 μs and a diffusion coefficient $D \approx 10^{-11}$ m^2 s^{-1} (31) result in signal reduction on the order of only one part in 10^7.

EXPERIMENTAL

The zeolite 4A sample was prepared by crushing industrial pellets, which, as a consequence of severe hydrothermal treatments, generally present lower diffusivities than laboratory prepared samples (2). Grains of 20–40 mesh (833–425 μm) were selected by sieving. A scanning electron microscope image of a crushed batch (Fig. 2) shows a particle size distribution between 1 and 5 μm. The sample was regenerated by oven drying at 573 K for 4 days. A 20.3% water load by weight was calculated based on the mass of the dry and hydrated samples, $m_{dry} = 2.3020$ g and $m_{hyd} = 2.7689$ g. A reference sample was prepared from the same sieved batch and hydrated by exposure to air at 287 $\pm$ 2 K and 40 $\pm$ 10% RH in an open glass dish for 2 weeks prior to the MRI experiment. Loosely packed zeolite (20 mm deep) and a reference sample (4 mm deep) were kept in a 14 mm diameter container as indicated in Fig. 3 and positioned in the radiofrequency (RF) probe. The
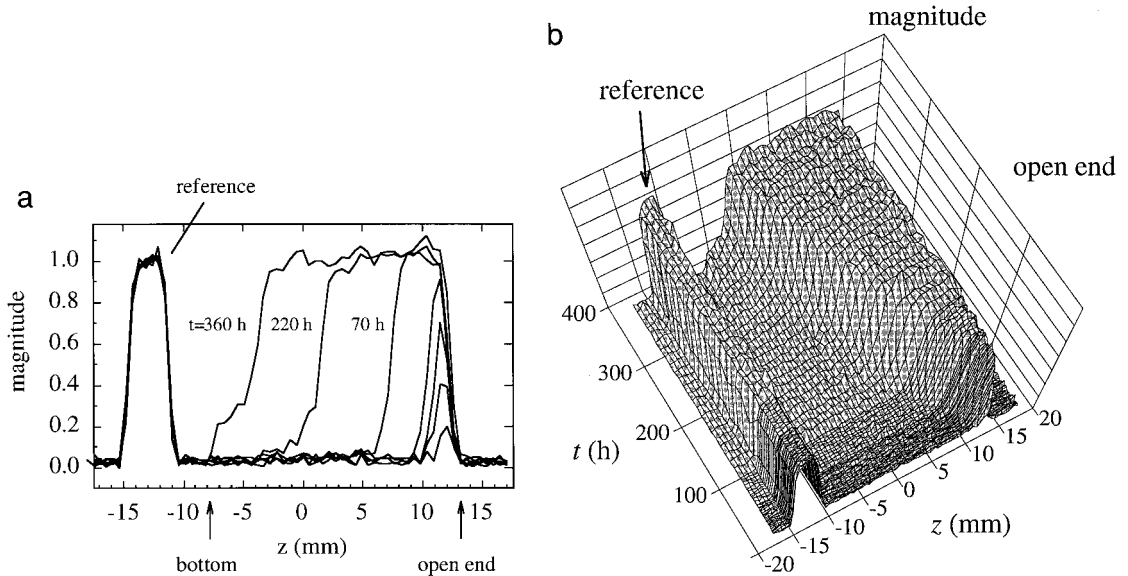

FIG. 4. One-dimensional magnitude profile showing the evolution of the sorption process. (a) Selected profiles and (b) complete data set. Magnitude has been normalized by integrated reference values.
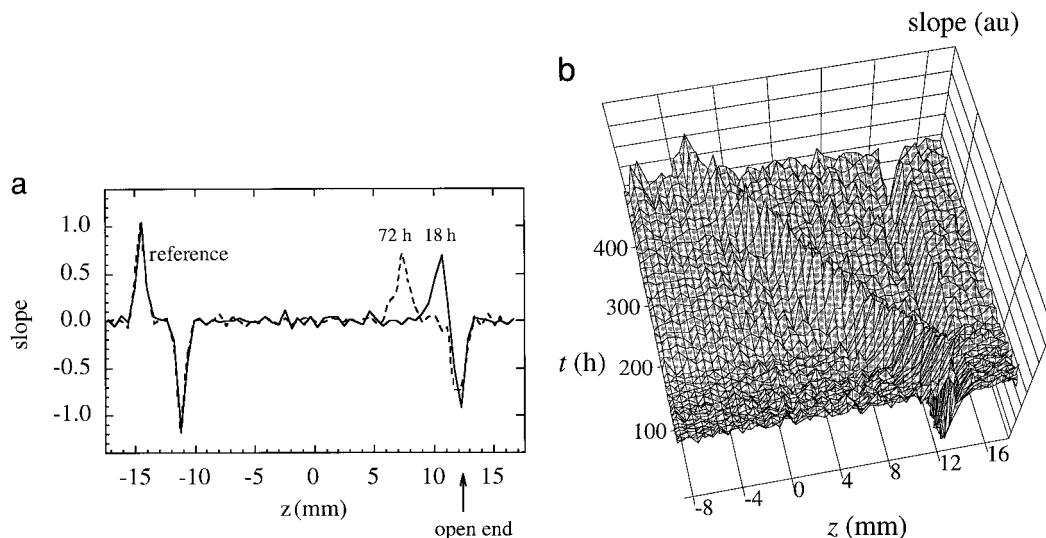
FIG. 5. Slope of the magnitude profiles calculated by the difference between neighboring points. (a) Results at 18 and 72 h. (b) Complete data set.

container and holders were made of Teflon to avoid spurious ^{1}H signal from plastic materials. The open end was covered with a thin cloth and exposed to ambient conditions. In order to maintain constant temperature and humidity conditions, the specimen was kept in the magnet bore at 283 ± 2 K and $40 \pm 10\%$ RH for the entirety of the experiment.

A homebuilt 32-rod birdcage resonator (*32*), in a 2.4-Tesla 32-cm horizontal bore superconducting magnet (Nalorac Cryogenics Inc., Martinez, CA) was used. The probe was driven by a 2kW RF amplifier (AMT, Brea, CA). A water-cooled 7.5 cm i.d. gradient set generated maximum gradients of 20 G/cm. Experiments were controlled by a Tecmag (Houston, TX) Libra S-16 console. Pulse sequence generation and data collection were controlled by MacNMR software.

1D SPRITE profiles composed of 64 points with a 35-mm FOV were achieved using an encoding time of 100 μs ($T_2^* \sim 300$ μs) and a maximum gradient of 20 G/cm. Gradient steps of 6-ms duration and a 4-μs RF excitation pulse were used. A simple AppleScript program launched groups of bulk and 1D-profile T_1, T_2, and T_2^* acquisitions at chosen adsorption times. The slow adsorption process permitted a large number of signal averages; 128 scans were collected per SPRITE profile in a total time of under 2 min. T_1 and T_2 mapping required longer SPI acquisitions, with a total time of about 40 min for 16 scans.

RESULTS AND DISCUSSION

Sorption Front Evolution

1D SPRITE magnitude profiles were obtained with 0.55 mm nominal resolution and then normalized by the reference signal integral, corresponding to 0.16 g/cm^{3} of water at 100% magnitude. For low hydration levels, data acquisition was per-

formed every 1.5 h and the time between runs was gradually increased, reaching 12 h by the second week of measurements. Some selected profiles are displayed in Fig. 4a. Figure 4b shows the complete data set in a stack-plot manner. Note that the adsorption front does not proceed into the zeolite bed until a high level of hydration is reached. The leading edge of the penetrating hydration front broadens slightly with time.

In order to estimate the velocity of the water adsorption front, the derivative of the magnitude profile was calculated as the difference between neighboring points. Results for two times are shown in Fig. 5a, while Fig. 5b displays the behavior of the front over the complete measured set.

The position of the maximum slope is used to mark the progress of the hydration front (Fig. 6). For small distances from the open end, the speed of the front is greater than observed deeper in the zeolite bed. The dashed line in Fig. 6 is a linear least squares fit using the first 80 hours of sorption. The calculated velocity in this range is 59 μm/h. As the water vapor
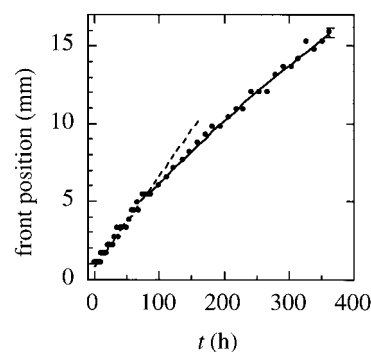

FIG. 6. Time evolution of the position of the slope maximum. The dashed line displays a linear regression based on the first 80 h of results. Solid line shows a second-order regression based on the data after 80 h.
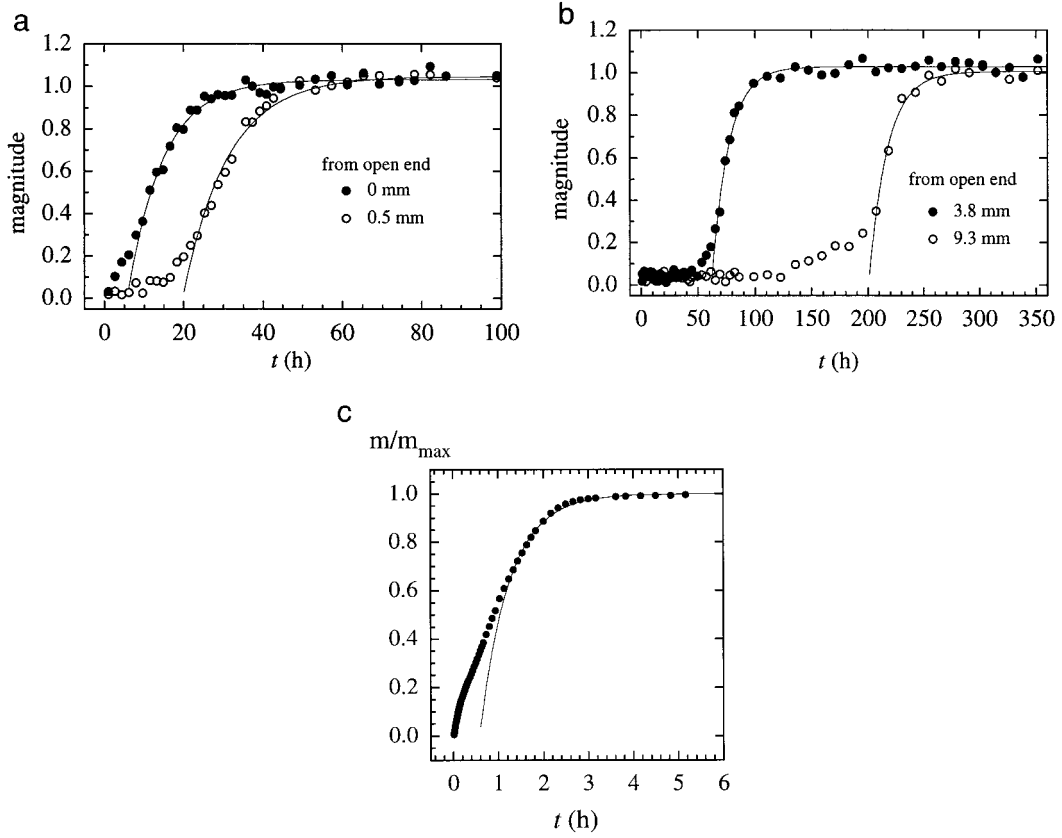
FIG. 7. Time evolution of the sorption process. Signal magnitude profiles normalized by reference sample: (a) hydration at the open end and 0.5 mm from the open end; (b) hydration deep in the zeolite bed. (c) Gravimetric results: normalized adsorbate mass. For all the results, least squares fits using high hydration levels are shown by solid lines.

molecules have to reach further points into the zeolite bed, the vapor supply rate at these points decreases, the front widens slightly, and the edge velocity is reduced. A second-order fit is shown by the solid line in Fig. 6. This behavior is in agreement with a rectangular or irreversible equilibrium isotherm for water vapor adsorption in zeolite 4A. Halse (27) has modeled water transport/adsorption through the zeolite powder, describing the dependence between the shape of the hydration profile and the vapor and intraparticle diffusion processes.

The hydration level has been studied at different positions. Figure 7 displays the time evolution of the normalized signal magnitude at four positions. A concentration of ~80% is reached in the open end before hydration proceeds to the adjacent pixel region. The adsorption approaches asymptotically the maximum concentration level, q_∞, in an exponential manner (2), then:

$$\frac{q}{q_\infty} \approx 1 - Ae^{-kt}, \qquad [5]$$

where k is the sorption rate constant or mass transfer coefficient and A is a model constant that contains information on the sorption triggering time and the particle shape. The low

concentration tails shown in the plots, which become more evident for points far from the open end (Fig. 7b), are a consequence of the competition of two processes: diffusion of the gas in the interparticle and intergrain space, and intraparticle diffusion (33, 34). Fitting of the uptake evolution profiles by an exponential increase is achieved by neglecting the low amplitude points. The mass transfer coefficients for two extreme cases (Figs. 7a and 7b) are 0.109 ± 0.006 h^{-1} for the open end, and 0.060 ± 0.005 h^{-1} for 9 mm deep in the zeolite bed. This behavior is compared with a gravimetric study performed on the same zeolite specimen, spreading the powder so that all grains have direct access to ambient air. Note that the

TABLE 1
T_1 Long and Short Recovery Contributions (Eq. [2]) for Partially Hydrated Sample[a]

	T_{1S} (ms)	A_S	T_{1L} (ms)	A_L
Bulk	9.5 ± 0.3	74%	36 ± 3	26%
Hydrated region	10 ± 1	84%	34 ± 14	16%
Hydrating front	9 ± 2	47%	42 ± 17	53%

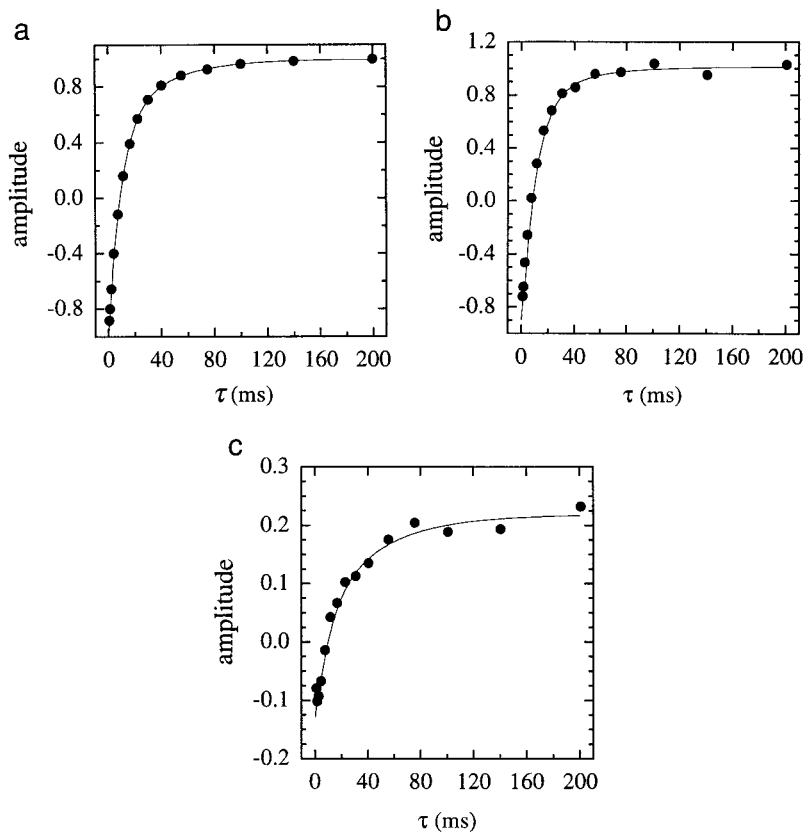[a] Results for bulk and two selected pixels after 255 h of sorption.

FIG. 8. Signal amplitude of the T_1 inversion recovery after 255 h of hydration. (a) Bulk data. (b) Average over the hydrated region. (c) Average over the hydrating front. Data have been normalized by integrated reference values. A double exponential least squares fit is displayed by the solid line.

time evolution of the adsorption (Fig. 7c) is similar to that of the MRI results, but with a higher rate, $k = 1.51 \pm 0.05$ h^{-1}, indicating the influence of the intergrain diffusion resistance when the powder is packed.

It should be stressed that magnitude values must be corrected for T_2^* variations with space. As demonstrated later, T_2^* varied little for high absorption levels.

Relaxation Time Mapping

T_1, T_2, and T_2^* mapping was performed during the uptake time evolution study. Complementary, bulk measurements of the relaxation times were attained in order to check for the existence of extra recovery or decay components. During the process, two T_1 contributions were clearly distinguished, while
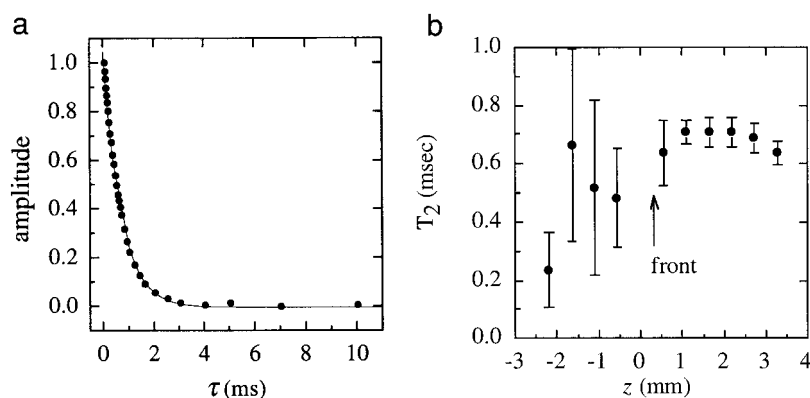

FIG. 9. T_2 echo amplitude decay for data at 255 h of hydration. (a) Bulk results. A single exponential least squares fit is displayed by the solid line. (b) Results for the hydration front region.
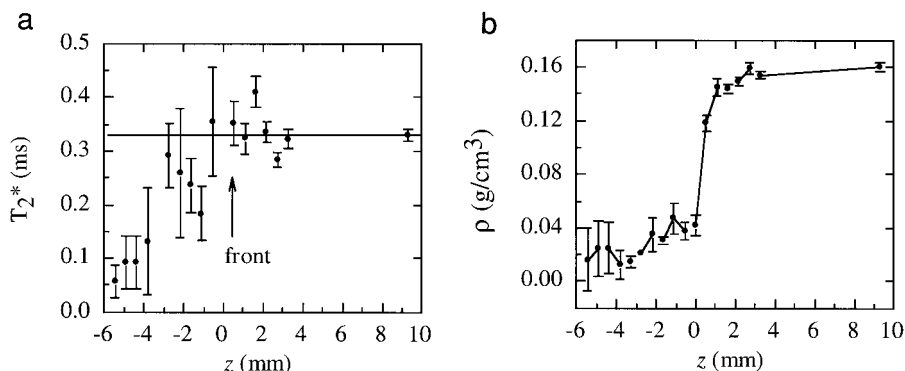
FIG. 10. Results for 255 h of hydration. (a) T_2^* single exponential decay fit and (b) true proton density (Eq. [4]).

T_2 and T_2^* remained single exponential. The analysis around the hydration front is of particular interest and is characterized by the appearance of a predominant long T_1 recovery and a short T_2^* decay.

The total time of hydration for the 2 cm sample is over 400 h. Figure 8a shows bulk T_1 inversion recovery for 255 h after the sorption experiment was initiated. Least square fitting to Eq. [2] showed the relative contributions from the long (A_L) and short (A_S) components. A general trend is observed for different positions along the profile. T_{1L} is predominant in the hydration front and the short time component remains unchanged. Results for bulk and two distinctive positions are presented in Table 1, and inversion recovery plots are displayed in Fig. 8b and Fig. 8c. Relative contributions are not significantly different along the hydrated region.

T_1 values reflect changes in mobility of the adsorbed water molecules as the hydration evolves. The predominance of a faster recovery in the hydrated section suggests that the molecules have localized in the zeolite cages. In the region of the concentration front, occupancy in the interparticle space is significant, as the intraparticle concentration builds up.

As seen on the bulk echo signal (Fig. 9a), T_2 is modeled by a single exponential decay, $T_2 = 663 \pm 6$ μs. Figure 9b shows a spatially resolved T_2 determination employing the spin echo sequence of Fig. 1b, 255 hours into the absorption experiment. No clear trend in T_2 is apparent along the hydration front. The large error bars are a consequence of low signal intensity in the low water concentration region ($c < 0.15$ c_∞). Other studies (3, 27) have reported two bulk T_2 components whose contributions depend on the hydration level. The single exponential behavior observed in the batch under investigation may be dictated by a dominant paramagnetic impurity effect.

T_2^* measurements reflect the molecular mobility in different environments, as described by high resolution NMR studies (35). Calculating the spin density (Eq. [4]), and T_2^* for individual pixels (Fig. 10a), reveals higher concentration values for the low signal intensity in the hydration front. T_2^* of 200 ± 20 μs was obtained by adding the signal from a 4-mm region of the adsorption front, while $T_2^* = 330 \pm 10$ μs in the hydrated

section of the zeolite bed. Figure 10b shows the space resolved water density, which has been calibrated by the known mass of adsorbate, as indicated previously. Note that the significant increase in SNR achieved by this SPRITE investigation, combined with T_2^* mapping, was necessary for a spatially resolved measurement of the adsorbate concentration.

CONCLUSIONS

The water adsorption process in a sample of zeolite 4A pellets has been studied by MRI methods. A technique which is able to observe short time constant signals (tens to hundreds of microseconds) was necessary to determine accurately the progress of the hydration front. The SPI and SPRITE MRI techniques were used, overcoming the restrictions of short transverse relaxation times and allowing for submillimetric resolution imaging.

The ability to perform relaxation time mapping (T_1, T_2, and T_2^*) in a nonequilibrated system has shown that this method can be used to investigate the water molecule mobility at the sorption front, which is clearly different from that of the hydration region. It should be noted that signal intensity profiles are not sufficient for modeling the sorption process. The true spin density must be calculated based on signal intensity and T_2^* mapping.

SPRITE water concentration profiles compared to gravimetric measurements determined that the sorption in a loosely packed zeolite bed with 20–40 mesh grains is 10 to 30 times slower than the uptake of spread grains.

ACKNOWLEDGMENTS

REFERENCES

1. R. T. Yang, "Gas Separation by Adsorption Processes," Imperial College Press, London (1997).

2. J. Kärger and D. M. Ruthven, "Diffusion in Zeolites and Other Microporous Solids," Wiley, New York (1992).

3. P. D. M. Hughes, P. J. McDonald, M. R. Halse, B. Leone, and E. G. Smith, *Phys. Rev. B* **51,** 11332 (1995).

4. D. M. Ruthven, "Principles of Adsorption and Adsorption Processes," Wiley, New York (1984).

5. J. Kärger and H. Pfeifer, *Magn. Reson. Imag.* **12,** 235 (1994).

6. J. Kärger, G. Seiffert, and F. Stallmach, *J. Magn. Reson. A* **102,** 327 (1993).

7. P. T. Callaghan, "Principles of Nuclear Magnetic Resonance Microscopy," Clarendon, Oxford (1991).

8. P. T. Callaghan and Y. Xia, *J. Magn. Reson.* **91,** 326 (1991).

9. B. Blümich and W. Kuhn (Eds.), "Magnetic Resonance Microscopy," VCH, Weinheim (1992).

10. M. L. Dickson, T. T. Norton, and E. Fernandez, *AIChE Journal* **43,** 409 (1997).

11. J. Kärger, N.-K. Bär, W. Heink, H. Pfeifer, and G. Seiffert, *Z. Naturforsch.* **50a,** 186 (1995).

12. J. Kärger, H. Pfeifer, M. Rauscher, and A. Walter, *J. Chem. Soc. Faraday Trans. I* **76,** 717 (1980).

13. P. J. McDonald, *Prog. NMR Spectrosc.* **30,** 69 (1997).

14. S. P. Cottrell, M. R. Halse, and J. H. Strange, *Meas. Sci. Technol.* **1,** 624 (1990).

15. J. J. Attard, P. J. McDonald, S. P. Roberts, and T. Taylor, *Magn. Reson. Imaging* **12,** 355 (1994).

16. M. J. D. Mallett, S. L. Codd, M. R. Halse, T. A. P. Green, and J. H. Strange, *J. Magn. Reson. A* **119,** 105 (1996).

17. S. Emid and J. H. N. Creyghton, *Physica* **128B,** 81 (1985).

18. D. E. Axelson, A. Kantzas, and T. Eads, *Can. J. Appl. Spectrosc.* **40,** 16 (1995).

19. S. D. Beyea, B. J. Balcom, P. J. Prado, A. R. Cross, C. B. Kennedy, R. L. Armstrong, and T. W. Bremner, *J. Magn. Reson.* **135,** 156 (1998).

20. P. J. Prado, B. J. Balcom, S. D. Beyea, T. W. Bremner, R. L. Armstrong, R. Pishe, and P. E. Grattan-Bellew, *J. Phys. D* **31,** 2040 (1998).

21. S. Choi, X.-W. Tang, and D. G. Cory, *J. Imaging Syst. Technol.* **8,** 263 (1997).

22. S. Gravina and D. G. Cory, *J. Magn. Reson. B* **104,** 53 (1994).

23. S. D. Beyea, B. J. Balcom, T. W. Bremner, P. J. Prado, D. P. Green, R. L. Armstrong, and P. E. Grattan-Bellew, *Cem. Concr. Res.* **28,** 453 (1998).

24. B. J. Balcom, R. P. MacGregor, S. D. Beyea, D. P. Green, R. L. Armstrong, and T. W. Bremner, *J. Magn. Reson. A* **123,** 131 (1996).

25. T. Meersmannn, G. Pavlosvskaya, A. Blue, S. Gibbs, M. Haake, and F. Cros, ENC Conference, Pacific Grove, California, abstract 272 (1998).

26. B. J. Balcom, in "Spatially Resolved Magnetic Resonance: Methods and Applications in Material Science, Agriculture and Biomedicine" (B. Blümich, R. Botto, and E. Fukushima, Eds.), Wiley/VCH, Weinheim (1998).

27. M. R. Halse, *Magn. Reson. Imag.* **14,** 745 (1996).

28. P. D. M. Hughes, P. J. McDonald, and E. G. Smith, *J. Magn. Reson. A* **121,** 147 (1996).

29. B. Leone, M. R. Halse, J. H. Strange, A. R. Lonergan, P. J. McDonald, and E. G. Smith, *Magn. Reson. Imag.* **12,** 247 (1994).

30. P. T. Callaghan, L. C. Forde, and C. J. Rofe, *J. Magn. Reson. B* **104,** 34 (1994).

31. J. Kärger, H. Pfeifer, M. Rosemann, N. N. Feokistova, and S. D. Zdanov, *Zeolites* **9,** 247 (1989).

32. C. E. Hayes, W. A. Edelstein, J. F. Schenck, O. M. Mueller, and M. Eash, *J. Magn. Reson.* **63,** 622 (1985).

33. J. Kärger and H. Pfeifer, *Zeolites* **7,** 90 (1987).

34. U. Rolle-Kampczyk, J. Kärger, J. Caro, M. Noack, P. Knlobes, and B. Röhl-Kuhn, *J. Colloids Interf. Sc.* **159,** 366 (1993).

35. U. Schwerk and D. Michel, *Colloids Surfaces A: Physicochem. Eng. Aspects* **115,** 267 (1996).